ADVANCED OPTICAL MATERIALS
www.advopticalmat.de

Near-Infrared Light Trapping and Avalanche Multiplication in Silicon Epitaxial Microcrystals

Virginia Falcone, Andrea Barzaghi, Fabio Signorelli, Joao Valente, Saleh Firoozabadi, Carlo Zucchetti, Roberto Bergamaschini, Andrea Ballabio, Federico Bottegoni, Franco Zappa, Francesco Montalenti, Leo Miglio, Kerstin Volz, Douglas J. Paul, Paolo Biagioni, Alberto Tosi, and Giovanni Isella*

The chemical vapor deposition of silicon on a patterned silicon substrate leads to the formation of 3D microcrystals, which, due to their inclined top facets and high aspect ratio, produce a light-trapping effect enhancing the optical absorption in the near-infrared (NIR). In this work, it is demonstrated that Si microcrystals can form the building blocks of a new class of NIR sensitive photodetectors operating in a linear or avalanche regime. Microcrystal-based devices are designed by coupling a 2D kinetic-growth model with a Poisson drift-diffusion solver and fabricated by combining electron beam lithography and low-energy plasma-enhanced chemical vapor deposition (LEPECVD). The optoelectronic properties of microcrystal-based *p–i–n* photodiodes are investigated both theoretically and experimentally by means of finite-difference time-domain (FDTD) simulations and responsivity measurements. At 1000 nm wavelength, the responsivity of microcrystal-based devices is six times higher than that of an equivalent mesa diode. Moreover, the photocurrent gains of Si microcrystals operating as an avalanche photodiode (APD), at the same wavelength, reaches 2×10^4 demonstrating the potentialities of substrate patterning, combined with epitaxial growth, for amplified photodetection applications.

1. Introduction

The indirect nature of the silicon band structure strongly limits the photon absorption at the energy gap threshold ($\lambda \approx 1100$ nm), lowering the NIR responsivity of silicon-based photodiodes (PD). Indeed, the NIR absorption coefficient of Si reduces by almost 67% moving from 700 to 1000 nm wavelength, thus hampering the exploitation of Si-based devices for wavelengths longer than ≈900 nm. Yet, infrared spectroscopy for biological/biomedical applications[1,2] or food analysis[3,4] would strongly benefit of photodetectors with an extended NIR sensitivity. Furthermore, many LiDAR[5] systems operate at 905 and 940 nm wavelengths and a more sensitive photodetector at those wavelengths allows an increase of the maximum operative distance for selected eye-safe laser power with a time-averaged value of 1 mW.

The use of smaller bandgap materials such Ge, GeSn alloys, or InGaAs can further extend the optical response range.[6–9]

V. Falcone, A. Barzaghi, A. Ballabio, G. Isella
L-NESS Dipartimento di Fisica
Politecnico di Milano
Via Anzani 42, Como I-22100, Italy
E-mail: virginia.falcone@polimi.it

F. Signorelli, F. Zappa, A. Tosi
Dipartimento di Elettronica
Informazione e Bioingegneria (DEIB)
Politecnico di Milano
Piazza Leonardo da Vinci 32, Milan 20133, Italy

J. Valente, D. J. Paul
James Watt School of Engineering
University of Glasgow
Rankine Building
Oakfield Avenue, Glasgow G12 8LT, UK

S. Firoozabadi, K. Volz
Materials Science Center and Department of Physics
Philipps-Universität Marburg
Hans-Meerweinstraße 6, 35032 Marburg, Germany

C. Zucchetti, F. Bottegoni, P. Biagioni
Dipartimento di Fisica
Politecnico di Milano
Piazza Leonardo da Vinci 32, Milano 20133, Italy

R. Bergamaschini, F. Montalenti, L. Miglio
L-NESS and Dipartimento di Scienza dei Materiali
Università di Milano-Bicocca
Milano I-20125, Italy

The ORCID identification number(s) for the author(s) of this article can be found under https://doi.org/10.1002/adom.202302568

DOI: 10.1002/adom.202302568

This has promoted the development of group IV and III–V devices for imaging[10] and telecommunication applications.[7] At the same time, a sufficiently large energy gap is required to sustain the avalanche multiplication of photocarrier, exploited in Si avalanche photodiodes (APD) to obtain an internal gain[11–13] exceeding 10^3. Ge[14,15] or InGaAs/InP[16,17] APDs typically require layer stacks featuring an absorption region separated from the avalanche region,[18,19] resulting in complex growth/fabrication procedures.

To enhance the photoresponse at long wavelengths (i.e., either in the NIR region for Si-based PD[20–23] or in the mid-infrared one for III–V based PD),[24] the development of micro-structured absorbing layers has also been explored. Several literature reports demonstrate that the surface texturing of silicon can enhance light absorption above 900 nm wavelength, and this can be implemented in silicon photodetectors operating either in the linear[20] or avalanche[22,25] regime. The most common micro structuring technique relies on femtosecond laser processing, resulting in the formation of random surface micro/nano spikes.[26–28] The surface texture achieved with this technique leads to an enhancement of NIR absorption with a maximum gain at 1000 nm of $\approx 10^3$, however, this has been reached for an APD thickness of several tens of micrometers.[22] An alternative approach consists of the top-down fabrication of either 2D light-diffraction elements,[25] combined with deep trenches and complex fabrication techniques, or an ordered array of nanowires,[29] exploiting waveguide modes and diffractive effects to obtain wavelength selective absorption,[30] typically at the expense of a poor fill factor.

Here, we propose a novel class of Si linear PDs and APDs based on epitaxial 3D microcrystals[31] featuring an extended NIR sensitivity. Such microcrystals are obtained by a mixed top-down/bottom-up approach exploiting optical or electron beam lithography for the patterning, on a Si substrate, of several μm-tall pillars and LEPECVD[32] for the epitaxial growth of dense microcrystal arrays. This technique has been used to avoid the crack formation and reduce extended defects in Ge,[33] 3C-SiC,[34] and GaAs[35] heteroepitaxy. In combination with composition grading[36] or electrochemical porosification,[37] full elastic relaxation of SiGe and Ge microcrystals have also been demonstrated. Moreover, 3D microcrystals have a height of several micrometers and are characterized by smooth faces and limited lateral expansion.[31]

In this work, we demonstrate that homoepitaxial Si microcrystals[38] can act as μm-sized linear and avalanche PDs with an increased NIR responsivity when compared to an equivalent Si planar or mesa diode. Finite-difference time-domain (FDTD) simulations have been used to analyze the light-trapping effect in faceted Si microcrystals forecasting an increased absorption in the NIR region as compared to a planar Si layer. This is confirmed by photocurrent measurements yielding a six-fold increase of the microcrystal responsivity, at 1000 nm wavelength, when compared with the reference mesa diode.

The microcrystal fabrication process allows the engineering of the doping profiles to enhance the photocurrent gain when operating in the avalanche multiplication regime. Indeed, APDs with an active region of 36 μm^2, low dark current (below 0.8 nA) and high gain (up to 2×10^4) at 1000 nm wavelength have been demonstrated. Such gain is obtained at room temperature, for a reverse-bias voltage lower than 40 V.

2. Substrate Patterning and Microcrystals Growth

Si microcrystals were obtained using a combined top-down/bottom-up approach. Arrays of square Si pillars, with an etch depth of 10 μm and a few micrometers lateral size, were fabricated by optical lithography and reactive ion etching starting from a 100 mm Si(001) wafer, *n*-type doped with an arsenic density of $\approx 1 \times 10^{19}$ cm^{-3}.

Twenty-four 1.5 × 1.5 cm^2 chips were patterned on a single wafer, each chip hosting fifteen patterns consisting of square Si pillars featuring different widths (W) and gaps (G) between adjacent pillars (see inset of **Figure 1c**). Si microcrystals were obtained by LEPECVD performed on the full patterned wafer using a deposition rate of 5 nm s^{-1} and a substrate temperature of 740°C for a total deposition thickness of 10 μm. Two different doping strategies were undertaken: in situ doping, using phosphorus, for *n*-type, and boron, for *p*-type doping or localized boron implantation as an alternative to *p*-type in situ doping.

A scanning electron microscopy (SEM) image of a microcrystal array is shown in Figure 1a, demonstrating the high fill factor and the morphological uniformity achieved due to the fine resolution of EBL patterning coupled with the stable and reproducible growth conditions in LEPECVD (as shown in, e.g., refs.[32,39,40,44]. Transmission electron microscopy (TEM) analysis was performed to study the evolution of crystal defects in such 3D microstructures. Figure 1b depicts a high-angle annular dark-field scanning transmission electron microscopy (HAADF-STEM) image of the interface between the patterned substrate and the grown Si microcrystal. The high-resolution HAADF-STEM image at the interface between the etched lateral side of the Si pillar shows twin boundaries, which are confirmed by the fast Fourier transform (FFT) of the image at the area of the Moiré fringes (for more details on the STEM analysis see the Methods section). However, crystal defects are expelled at the lateral surface and do not reach the main body of the microcrystal, which acts as the light absorbing element in our devices.

Figure 1c shows how the pattern geometrical properties influence the final morphology of 3D microcrystals obtained in the same deposition run, i.e. under identical growth conditions. For all cases shown in Figure 1c the microcrystal top surface is predominately formed by {001}, {111}, and {113} facets, however, the relative size of the different facets depends on the characteristic dimensions of the pattern as analyzed in detail in refs. [39,40]. For our purposes we will consider two main groups of microcrystals that can be classified as "predominantly faceted" or "predominantly flat". In predominantly faceted microcrystals, the top surface is dominated by {111} and {113} facets, while predominantly flat microcrystals are characterized by a relatively large (001) facet. This classification can be made quantitative by introducing a degree of faceting defined as:

$$D_{\mathrm{fac}} = \frac{S_{\mathrm{tot}} - S_{001}}{S_{\mathrm{tot}}} \quad (1)$$

where S_{tot} is the projected area of the top surface of the microcrystal on the plane normal to the [001] direction, while S_{001} is the area of the (001) facet. In the following, we will indicate predominantly faceted microcrystals with $D_{\mathrm{fac}} > 90\%$ and predominantly flat those with $D_{\mathrm{fac}} < 90\%$. As shown in Figure 1c the patterns

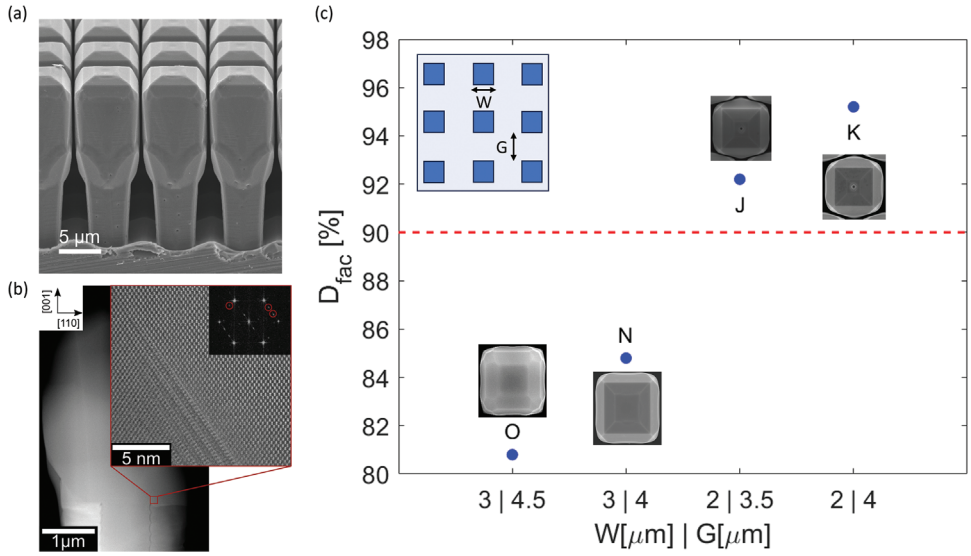

Figure 1. Microcrystals morphology: a) side-view SEM image of the 3D Si microcrystals grown on a patterned Si substrate featuring W = 3 μm and G = 4 μm; b) HAADF image taken at the center of a Si microcrystal grown on a patterned Si substrate, with dimensions W = 1 μm and G = 3 μm. A high-resolution HAADF image depicts the epilayer/substrate interface. The FFT of the high-resolution image is included as an inset; c) dependence of the degree of faceting of microcrystals on the substrate patterning.

indicated by the letters O and N can be considered as predominantly flat, patterns J and K as predominantly faceted.

3. Modeling of Microcrystals Electronic Properties

At variance with conventional vertically-illuminated detectors, microcrystal-based PD are inherently nonplanar. This means that in addition to the final faceted morphology, PDs, and APDs need to be designed considering facets evolution during growth and the ensuing nonplanar distribution of donors or acceptors during in situ doping.

The modeling of microcrystal growth can be addressed by the rate equations approach, detailed in refs. [39,40], taking into account the combined effect of the local deposition flux, subject to mutual shielding between adjacent microcrystals, and the facet-dependent incorporation rates, fitted from experimental data (see Supporting Information). The time integration of the rate equations, here limited to the 2D {110} cross-section for numerical convenience, offers a reliable reconstruction of the evolution of the microcrystal profile during growth, consistent with both experiments and more advanced 3D simulations.[36] **Figure 2**a,b shows the facet evolution during deposition, as obtained from the simulations, superposed on the final microcrystal morphology, as obtained from SEM, for the case of microcrystals K and N, respectively.

The in situ doping profile is shown in Figure 2c. The bottom part of the microcrystal consists of a 6 μm thick *n*-type region (phosphorous concentration $\approx 2 \times 10^{18}$ cm^{-3}) terminated by a decreasing half-Gaussian concentration profile. The depleted zone is mainly formed within a 3.8 μm thick *p*-type region doped with a boron concentration smoothly decreasing from 1.65 to 1.5×10^{16} cm^{-3}. In situ doped microcrystals are terminated by a 200 nm *p*-type top contact (boron concentration $\approx 1 \times 10^{19}$ cm^{-3}). A sketch of the electric field profile, resulting from the in situ doping, is shown in Figure 2d highlighting the high-field multiplication region and the low-field absorption region. In the implanted samples, the top 200 nm have been left nominally undoped during growth, and only the 2×2 μm^2 central region of the microcrystal top has been doped by implanting boron with a dose of 10^{15} cm^{-2}, at 6 keV energy, 7° tilt and 20° rotation. The resulting estimated peak boron concentration at the surface is $\approx 2.5 \times 10^{20}$ cm^{-3} for an approximate depth of 50 nm. More details on the implantation procedure can be found in Methods.

The electrical properties of the in situ doped and the implanted microcrystals were modeled using the Synopsys Sentaurus TCAD software taking the 2D morphological evolution and doping profile as the input parameters. In this way, it is possible to calculate the 2D electric field distribution within the microcrystals. Figure 2e shows the doping and electric field map for an in situ doped N microcrystal. The results for the implanted case are shown in Figure 2f. We notice that the electric field for the in situ doped microcrystal, Figure 2e, features "hot spots" close to the microcrystal edges, where the avalanche multiplication results are much higher. These hot spots are generated from the in situ doped "shell" profile (Figure 2e left side) generated by surface diffusion and by the mutual shadowing taking place during the microcrystal's growth. When the reverse bias voltage of the *p-n* junction increases, the dark current progressively increases due to the stronger carrier generation, and the electric field hot-spots lead to an even steeper increase, also because we expect more defects, acting as generation centers, close to the microcrystal sidewalls. As a consequence, the breakdown transition is less sharp and the breakdown voltage itself is lower (see Figure 2g,h, in situ curves). This effect is typically called "edge breakdown" and forces it to operate the APD at lower bias voltage,[18,41] thus reducing the avalanche gain at the center of the microcrystal. Instead, the electric field distribution obtained for the implanted microcrystal, Figure 2f, appears to

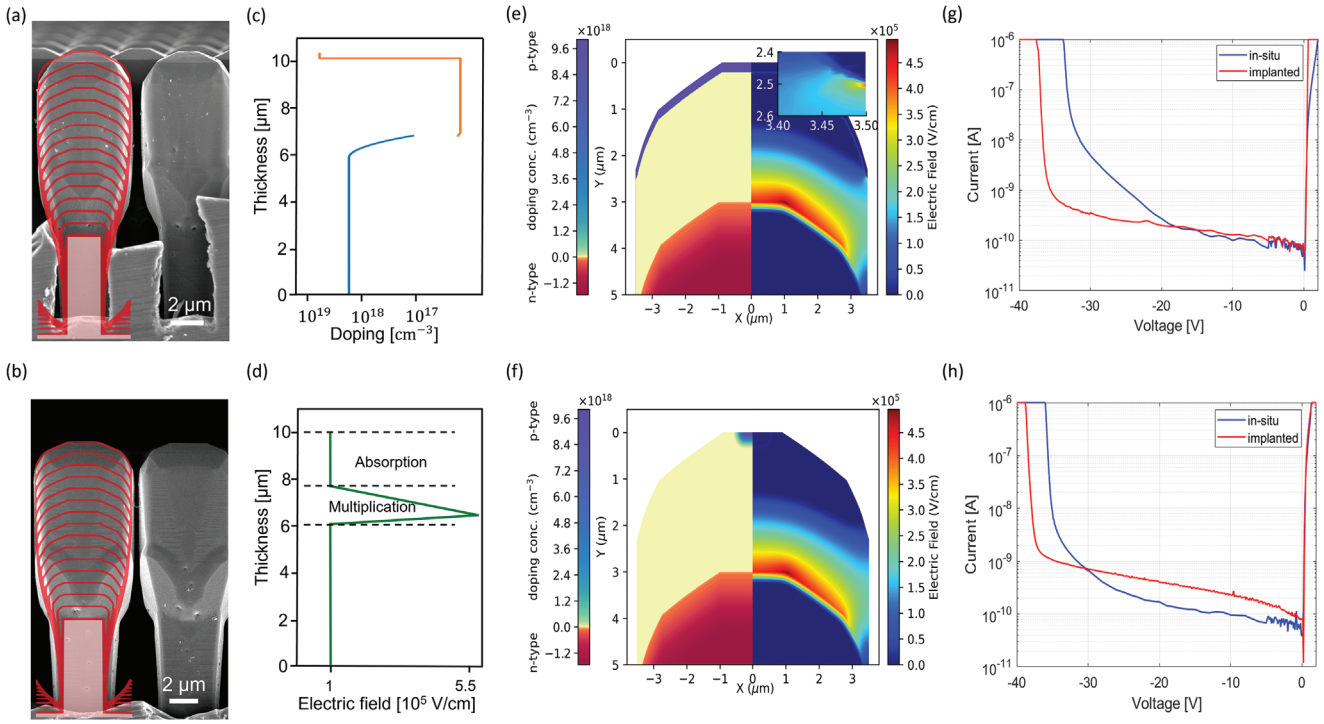

Figure 2. Microcrystal doping and current–voltage characteristics: a,b) facet evolution during growth for a) K and b) N microcrystals. c) Doping profile for in situ doped microcrystal, the Si pillar/Si microcrystal interface has been taken as a reference point for the microcrystal height. The orange curve represents the *p*-doping, while the blue one the *n*-doping. d) A schematic diagram of the electric field expected from the doping profile shown in (c). e,f) The simulated doping profile and electric field distribution for in situ doped e) and implanted f) microcrystals. g,h) A comparison of the dark current measured for implanted and in situ doped g) K and h) N microcrystals.

be well confined within the microcrystal without any evident hot spot, thus leading to sharper breakdown transition and higher breakdown voltage (see Figure 2g,h, implanted curves).

In detail, Figure 2g,h shows the current–voltage *(I–V)* curves from individual K and N microcrystals, respectively, both in situ doped and implanted. The dark *I–V* curves were acquired, at room temperature, by landing a nanotip on the microcrystal top and using the wafer back-side as the bottom contact (for more details on the experimental set-up see the Methods section). To check the uniformity within the pattern and evaluate the variability introduced by the nanotip landing process, different microcrystals have been measured obtaining comparable results. An overview of the *I–V* curves measured for microcrystals of the same pattern is reported in the Supporting Information.

We notice that in all cases a dark current of hundreds of pA is observed at low reverse bias, however, implanted microcrystals feature a sharp breakdown at ≈ −38 V, while in the case of in situ doped microcrystal the breakdown is gradually reached for lower reverse bias voltage. As mentioned, this behavior is consistent with the presence of electric-field hot spots for the in situ doped microcrystals (see Figure 2e) and we conclude that implanted microcrystals are more suitable for operation as APDs.

4. Light Trapping in Si Microcrystals

2D FDTD simulations were implemented, using the Ansys Lumerical FDTD software, to investigate the optical properties of Si microcrystals. A typical simulation domain is shown in Figure 3a. The morphology of the microcrystal was reconstructed starting from cross-section SEM images and a plane wave was used to model the top-illumination condition. Periodic boundary conditions along the horizontal direction have been imposed to take into account the pattern periodicity, while perfectly matched layers were used to suppress any light back-propagating from the top and bottom boundaries of the simulation domain.

The absorbed power density spatial maps at 600 and 900 nm wavelengths, for the N microcrystal, are shown in Figure 3b,c, respectively. In both cases the inclined top facets of the microcrystal yield a light-trapping effect, increasing the optical path inside the microcrystal.[42–45] This effect is more pronounced in the NIR region (e.g. 900 nm – Figure 3c), where the absorption coefficient of silicon is lower, thus leading to a longer optical path within the microcrystal and multiple internal reflections. Additional optical simulation results can be found in the Supporting Information.

To highlight the role played by the light-trapping effect in the microcrystal-based PD, the spectral dependence of the total absorbed power of K (Figure 3d) and N (Figure 3e) microcrystals was compared with that of a planar Si layer, featuring the same total thickness. We notice that for both microcrystals, the faceted morphology increases the total absorbed power over that of the planar layer. This effect is particularly pronounced in the NIR region where a twofold enhancement is expected, moreover, the predominantly faceted microcrystal K, features a stronger NIR absorption as compared to the predominantly flat N microcrystal.

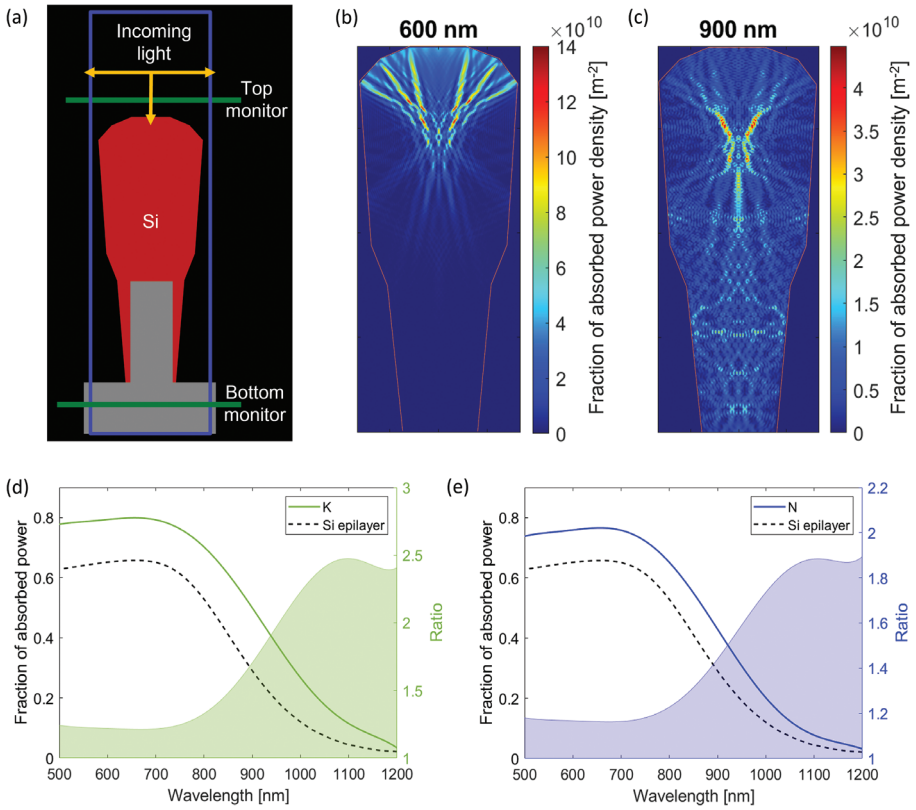

Figure 3. Light-trapping effect in Si microcrystals. a) The simulation domain used for FDTD calculations; b,c) absorption maps at 600 and 900 nm wavelengths for N microcrystals; d,e) a comparison between the fraction of power absorbed by d) K and e) N microcrystals and by a reference Si layer. In both panels the ratio of the power absorbed by the microcrystal and by the reference layer is shown on the right axis.

5. Electro-Optical Characterization of Si Microcrystals

The electro-optical characterization of the microcrystal-based PDs was performed using a confocal microscope and a monochromatized supercontinuum laser to obtain a spot size of ≈7 μm and a typical optical power of ≈10 μW. The current was collected by means of a nanotip (top contact) and an Ohmic contact formed on the back side of the *n*-type Si wafer (bottom contact). The photocurrent was measured by taking the difference between the current under illumination and in dark conditions. More details on the photocurrent measurement set-up can be found in the Methods section.

The same set-up was used also to characterize a vertically illuminated photodiode, obtained by etching a 100 μm diameter mesa from the unpatterned region of the same Si wafer used for the microcrystal growth. As a consequence, such a mesa PD features exactly the same growth condition and doping profile of in situ doped microcrystals and was used as a reference to estimate the impact of the microcrystal morphology on the photoresponse.

Figure 4 reports the responsivity of the K and N microcrystals, both in situ doped and with an implanted top contact, at different reverse biases. By comparing the photoresponse of the K microcrystals (Figure 4a,b) with that of the N microcrystals (Figure 4c,d) we notice that their morphology strongly influences the spectral dependence of the photocurrent. Figure 4e,f shows a direct comparison between the reference and the microcrystal-based PDs. The NIR responsivity of the K and N micro-PD outperforms that of the reference PD, with the ratio between the microcrystal/planar photoresponse closely resembling the simulated absorption ratio reported in Figure 3d,e. The NIR responsivity enhancement, experimentally measured in the micro-PDs, is larger than what was expected solely from the absorption calculations (see Figure 3d,e). Indeed, the photoresponse is determined also by the photocarrier collection efficiency, which appears, therefore, to be larger in the 3D microcrystals than in the planar, reference PD. Such an interplay between absorbed power density and collection efficiency might also be the reason for the different experimental spectral response of K and N devices, which has no clear counterpart in the FDTD simulations.

In Figure 4a–d there is a clear non-linear dependence of the responsivity on the reverse bias with a strong photoresponse increase as the bias approaches the breakdown voltage. This is a clear indication of avalanche gain, which was more accurately investigated by reducing the impinging optical power to the nW range.

The dark and illuminated *I*–*V* curves, at four selected wavelengths (700, 800, 900 and 1000 nm), are shown in **Figure 5**a,b for implanted K and N microcrystals, respectively. The photocurrent gain of an APD device can be defined as [46]:

$$G = \frac{I_{ph}(V)}{I_{ph}(V_0)} \quad (2)$$

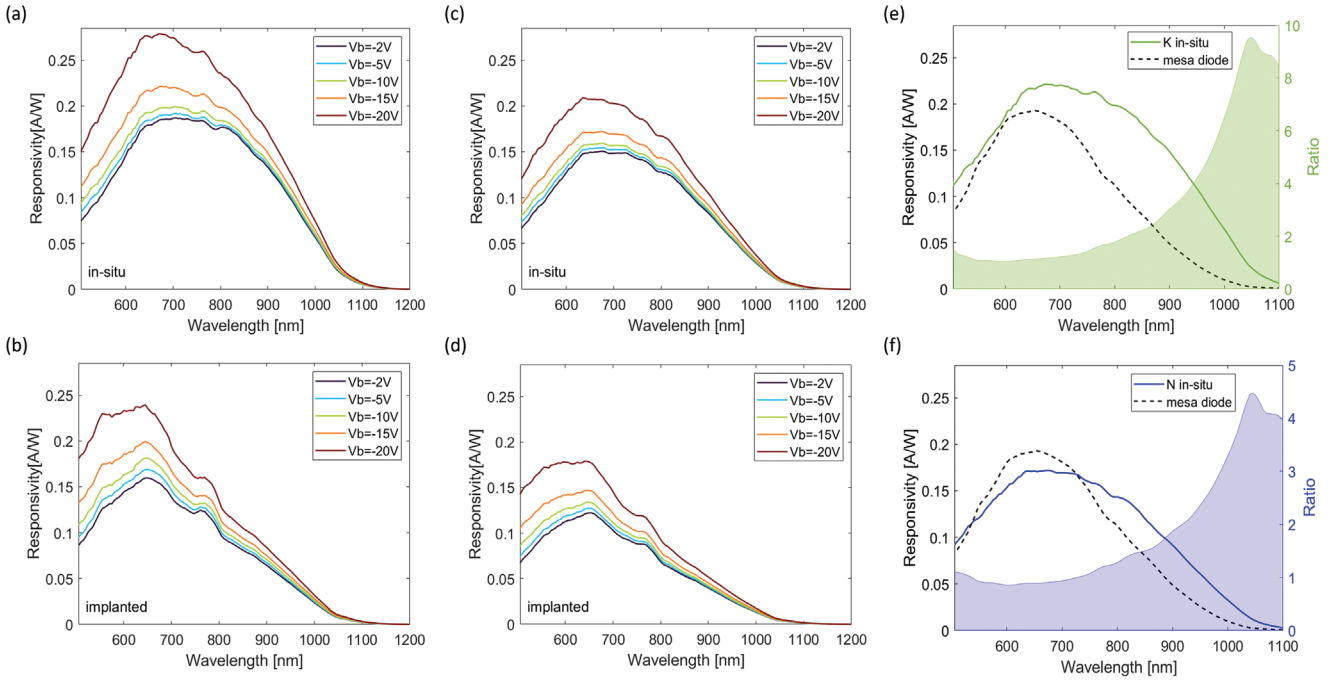

Figure 4. Responsivity of microcrystal based PDs: a,b) responsivity of K microcrystal obtained by a) in situ doping and b) implantation; c,d) responsivity of N microcrystal obtained by c) in situ doping and d) implantation; e,f) comparison between the photoresponse of e) in situ doped K and f) N microcrystals and the reference mesa diode.

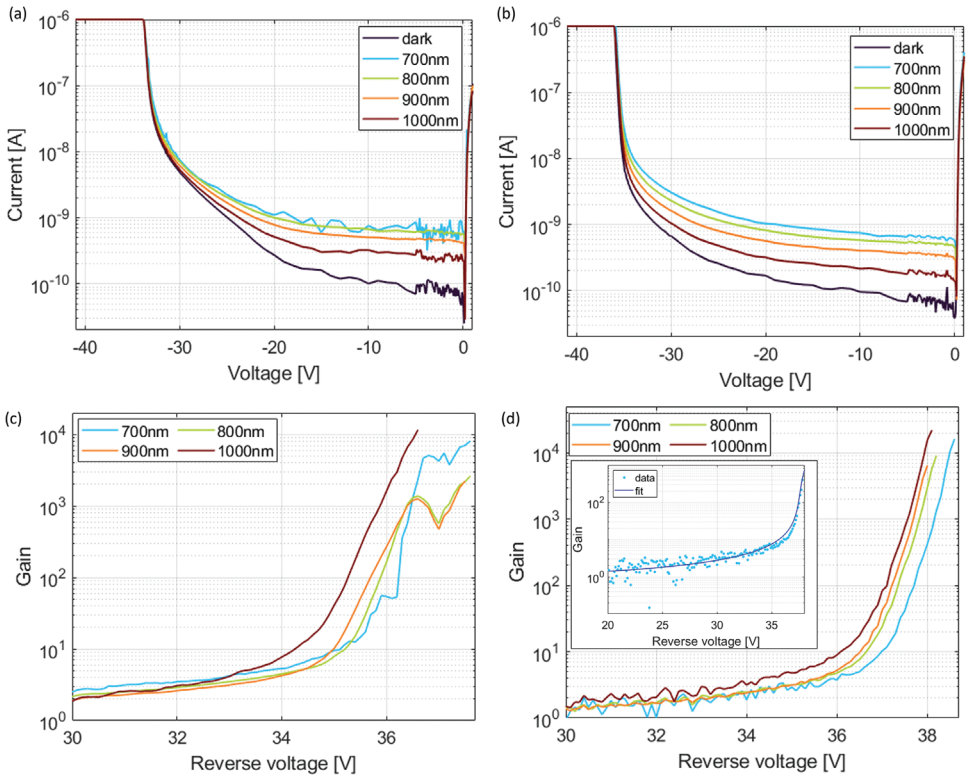

Figure 5. The avalanche gain in the Si microcrystals at room temperature: a,b) the current under monochromatic illumination and in dark conditions in a) K and b) N microcrystals. All measurements were normalized for an equal incident power of 4 nW. c,d) Avalanche gain in c) K and d) N microcrystals.

with $I_{ph}(V)$ the bias-dependent photocurrent and $I_{ph}(V_0)$ the photocurrent at a reference voltage V_0, where the avalanche phenomena are negligibly small. By applying Equation (2) to the photocurrent curves and taking $V_0 = -3$ V we obtained the avalanche gain factor reported in Figure 5c,d. Gain exceeding 10^3 (Figure 5c) and 10^4 (Figure 5d) are observed for K and N microcrystals, respectively. It can be noticed that larger gains are systematically obtained at longer wavelengths despite a clear decrease of the responsivity in the 700–1000 nm range. This behavior can be attributed to the interplay between the light-trapping effect and the electric field distribution within the microcrystals. Indeed, the long wavelength radiation is more efficiently confined within the microcrystal (see Figure 3b,c), where the electric field is more intense (see Figure 2e,f) resulting in a higher gain. The maximum gain of 2×10^4 is reached at 1000 nm wavelength for N microcrystals.

The experimental data obtained at 700 nm wavelength were fitted with a semi-empirical expression[46] describing the avalanche process as shown in the inset of Figure 5d, thus confirming the physical origin of the observed gain. More details on the fitting procedure can be found in the Methods section.

6. Conclusion

In summary, we demonstrate that the enhanced absorption taking place in the 3D microcrystals can be exploited to increase the NIR responsivity of Si PDs and APDs. As predicted by FDTD simulations and confirmed by photocurrent measurements, the light-trapping effect takes place within the faceted Si microcrystals, thus enhancing the optical path of the impinging light. Electrical simulations were developed to investigate the electric field distribution in the in situ doped and implanted microcrystals. While in situ doping results in linear PD with a higher NIR responsivity, implanted microcrystals are more suitable for operation as APD thanks to their sharper breakdown behavior and lower dark currents close to breakdown. The responsivity obtained for the microcrystal-based PDs operating in the linear regime exceeds by a factor of six the one of an equivalent Si mesa diode at 1000 nm wavelength without any sizeable reduction at wavelengths below 900 nm. Gain up to 2×10^4 was obtained for an incident wavelength of 1000 nm in the microcrystal APDs. These results demonstrate the potential of a new class of PD devices based on microcrystals epitaxially grown on patterned substrates.

7. Experimental Section

HAADF-STEM Images: A cross-sectional, electron transparent sample was prepared at the center of microcrystals along the [110] crystallographic orientation. It was achieved through mechanical polishing using sandpapers (MultiPrepTM System 8″, Allied High Tech Products Inc., Rancho Dominguez, CA, United States), as well as Ar-ion milling using a PIPS machine (PIPS, Gatan, Inc., Pleasanton, CA, United States).[47,48]

A double Cs-corrected scanning transmission electron microscope (Jeol Ltd., Tokyo, Japan), operating at an acceleration voltage of 200 kV, was employed to capture HAADF-STEM micrographs. The sub-Angstrom probe size achievable by this instrument enabled atomic-resolution characterization of the sample.

Doping Profile: The doping profile represented in Figure 2c was engineered to achieve a high electric field distribution inside the microcrystals, as shown in Figure 2d, required for its functionality as an Avalanche Photodiode (APD). Below the top 200 nm of *p*++ contact, a low *p*-doping region was present to work as an absorption region. The photogenerated electrons would then enter the multiplication region formed at the junction between *p*-doped and *n*++ doped regions, triggering the internal gain mechanism of the Si microcrystals APDs.

A comparison between the nominal and experimentally measured doping profile is shown in Figure S5 (Supporting Information).

Implantation: The top contact implantation required a series of fabrication steps. An oxide passivation layer was deposited by atomic layer deposition and annealed in forming gas at 360°C. Then 20 µm of SiO_2 was deposited by plasma-enhanced CVD to form a planarization layer which was then thinned by chemical mechanical polishing to reach the top of the microcrystals. Electron beam lithography was used to define the implantation area where a final buffered-HF etching was performed to leave a few nanometers thick oxide layer. Boron implantation was performed using a 1×10^{15} cm^{-2} dose at 6 keV, 7° tilt, and 20° rotation. Dopant activation was achieved by means of a 50 s annealing at 950 °C.

I–V and Photocurrent Experimental Set-Up: The dark and illuminated characteristics of individual microcrystals were obtained by combining a confocal microscope[44,45] and a nanoprobe. A schematic representation of the experimental set-up can be found in the Supporting Information.

A monochromatized supercontinuum laser (SuperK Extreme EXW-12, NKT Photonics) with a wavelength FWHM of ≈10 meV was used to excite photocarriers in the wavelength range between 500 and 1200 nm. An objective with a 0.7 numerical aperture was used to obtain a 7 µm diameter light spot with a power distribution almost uniform inside the spot area.

A nanoprobe from Kleindiek Nanotechnik equipped with a tungsten tip with a radius of 100 nm was used to establish electrical contact with individual microcrystals, while the bottom surface of the sample was used as a bottom contact.

Gain Data Fitting: The avalanche gain *G* dependence on the applied reverse bias *V* can be expressed as:

$$1 - \frac{1}{G} = \left[\frac{V - \left(I_d\left(V_0\right) + I_{ph}\left(V_0\right) \right) R\, G}{V_{BD}} \right]^n \tag{3}$$

where V_{BD} is the breakdown voltage, R is the diode series resistance, $I_d(V_0)$ and $I_{ph}(V_0)$ are the dark and photocurrent at the reference voltage V_0, and n is a fitting parameter.[46]

This transcendental equation was solved by setting $I_d\ (V_0) = 1 \times 10^{-10}$ A, $R = 900$ kΩ and keeping n and V_{BD} as free parameters. The value of the equivalent resistance was obtained by a linear fit of the *I–V* curve in the forward voltage region. The semi-empirical gain curve and the experimental one for an incident wavelength of 700 nm is shown in the inset of Figure 5d. The model fits well with the experimental data with an estimated value of $n = 2$ and of the breakdown voltage equal to 37.9 V.

Supporting Information

Supporting Information is available from the Wiley Online Library or from the author.

Acknowledgements

This research was funded by the European Commission (Horizon-2020 FET "microSPIRE" project, ID: 766955). DJP acknowledges funding from the Royal Academy of Engineering (CiET2021\123). The authors acknowledge Enrico Napolitani for the SIMS measurement presented in the Supporting Information.

Conflict of Interest

The authors declare no conflict of interest.

Data Availability Statement

The data that support the findings of this study are available from the corresponding author upon reasonable request.

Keywords

avalanche multiplication, light trapping, near-infrared detectors, silicon epitaxial microcrystals

Received: October 10, 2023
Revised: February 27, 2024
Published online:

[1] M. Lin, M. Al-Holy, M. Mousavi-Hesary, H. Al-Qadiri, A. G. Cavinato, B. A. Rasco, *Letters in Applied Microbiology* **2004**, *39*, 148.
[2] K. B. Beć, J. Grabska, C. W. Huck, *Molecules* **2020**, *25*, 2948.
[3] Q. Fu, J. Wang, G. Lin, H. Suo, C. Zhao, *J. Anal. Methods Chem.* **2012**, *2012*, 728128.
[4] M. G. G. Awanthi, B. M. S. Jinendra, S. B. Navaratne, C. M. Navaratne, *Journal of Cereal Science* **2019**, *89*, 102795.
[5] X. Sun, L. Zhang, Q. Zang, W. Zhang, *Appl. Sci.* **2019**, *9*, 4225.
[6] I. A. Fischer, M. Brehm, M. De Seta, G. Isella, D. J. Paul, M. Virgilio, G. Capellini, *APL Photonics* **2022**, *7*, 050901.
[7] S. Famà, L. Colace, G. Masini, G. Assanto, H.-C. Luan, *Appl. Phys. Lett.* **2002**, *81*, 586.
[8] N. Koompai, T. H. N. Nguyen, V. Turpaud, J. Frigerio, V. Falcone, S. Calcaterra, L. Lucia, A. Bousseksou, R. Colombelli, J.-R. Coudevylle, D. Bouville, C. Alonso-Ramos, L. Vivien, G. Isella, D. Marris-Morini, *Appl. Phys. Lett.* **2023**, *123*, 031109.
[9] M. M. Ballester, L. Deniel, N. Koompai, T. H. N. Nguyen, J. Frigerio, A. Ballabio, V. Falcone, X. Le Roux, C. Alonso-Ramos, L. Vivien, A. Bousseksou, G. Isella, D. Marris-Morini, *ACS Photonics* **2022**, *9*, 249.
[10] E. Talamas Simola, V. Kiyek, A. Ballabio, V. Schlykow, J. Frigerio, C. Zucchetti, A. De Iacovo, L. Colace, Y. Yamamoto, G. Capellini, D. Grützmacher, D. Buca, G. Isella, *ACS Photonics* **2021**, *8*, 2166.
[11] M.-J. Lee, W.-Y. Choi, *Opt. Express* **2010**, *18*, 24189.
[12] H.-S. Kang, M.-J. Lee, W.-Y. Choi, *Appl. Phys. Lett.* **2007**, *90*, 151118.
[13] M.-J. Lee, H. Rucker, W.-Y. Choi, *IEEE Electron Device Lett.* **2011**, *33*, 80.
[14] S. Wu, H. Zhou, L. He, Z. Wang, Q. Chen, L. Zhang, C. Seng, *IEEE Sens. J.* **2023**.
[15] Y. Kang, H.-D. Liu, M. Morse, M. J. Paniccia, M. Zadka, S. Litski, G. Sarid, A. Pauchard, Y.-H. Kuo, H.-W. Chen, W. S. Zaoui, J. E. Bowers, A. Beling, D. C. McIntosh, X. Zheng, J. C. Campbell, *Nat. Photonics* **2009**, *3*, 59.
[16] C. Liu, H.-F. Ye, Y-Li Shi, *Chip* **2022**, *1*, 100005.
[17] F. Signorelli, F. Telesca, E. Conca, A. Della Frera, A. Ruggeri, A. Giudice, A. Tosi, *IEEE J. Sel. Top. Quantum Electron.* **2022**, *28*, 1.
[18] P. Vines, K. Kuzmenko, J. Kirdoda, D. C. S. Dumas, M. M. Mirza, R. W. Millar, D. J. Paul, G. S. Buller, *Nature Comms.* **2019**, *10*, 1086.
[19] M. Ren, S. J. Maddox, M. E. Woodson, Y. Chen, S. R. Bank, J. C. Campbell, *Appl. Phys. Lett.* **2016**, *108*, 191108.
[20] J. E. Carey, C. H. Crouch, M. Shen, E. Mazur, *Opt. Lett.* **2005**, *30*, 1773.
[21] C. Wu, C. H. Crouch, L. Zhao, J. E. Carey, R. Younkin, J. A. Levinson, E. Mazur, R. M. Farrell, P. Gothoskar, A. Karger, *Appl. Phys. Lett.* **2001**, *78*, 1850.
[22] R. A. Myers, R. Farrell, A. M. Karger, J. E. Carey, E. Mazur, *Appl. Opt.* **2006**, *45*, 8825.
[23] A. Ono, K. Hashimoto, N. Teranishi, *Opt. Express* **2021**, *29*, 21313.
[24] D. Chen, S. D. March, A. H. Jones, Y. Shen, A. A. Dadey, K. Sun, J. A. McArthur, A. M. Skipper, X. Xue, B. Guo, J. Bai, S. R. Bank, J. C. Campbell, *Nat. Photon.* **2023**, *17*, 594.
[25] S. Shimada, Y. Otake, S. Yoshida, S. Endo, R. Nakamura, H. Tsugawa, T. Ogita, T. Ogasahara, K. Yokochi, Y. Inoue, K. Takabayashi, H. Maeda, K. Yamamoto, M. Ono, S. Matsumoto, H. Hiyama, T. Wakano, IEEE International Electron Devices Meeting (IEDM), IEEE, San Francisco, CA, USA, **2021**.
[26] T.-H. Her, R. J. Finlay, C. Wu, S. Deliwala, E. Mazur, *Appl. Phys. Lett.* **1998**, *73*, 1673.
[27] T.-H. Her, R. J. Finlay, C. Wu, E. Mazur, *Appl. Phys. A* **2000**, *70*, 383.
[28] A. J. Pedraza, J. D Fowlkes, D. H. Lowndes, *Appl. Phys. Lett* **1999**, *74*, 2322.
[29] T. Bartschmid, F. J. Wendisch, A. Farhadi, G. R. Bourret, *ACS Appl. Energy Mater.* **2022**, *5*, 5307.
[30] K. Seo, M. Wober, P. Steinvurzel, E. Schonbrun, Y. Dan, T. Ellenbogen, K. B. Crozier, *Nano Lett.* **2011**, *11*, 1851.
[31] C. Falub, H. von Känel, F. Isa, R. Bergamaschini, A. Marzegalli, D. Chrastina, G. Isella, E. Müller, P. Niedermann, L. Miglio, *Science* **2012**, *335*, 1330.
[32] C. Rosenblad, H. R. Deller, A. Dommann, T. Meyer, P. Schroeter, H. von Känel, *J. Vac. Sci. Technol. A* **1998**, *16*, 2785.
[33] A. Marzegalli, F. Isa, H. Groiss, E. Müller, C. V. Falub, A. G. Taboada, P. Niedermann, G. Isella, F. Schäffler, F. Montalenti, H. von Känel, L. Miglio, *Adv. Mater.* **2013**, *25*, 4408.
[34] M. Agati, Boninelli, C. Calabretta, F. Mancarella, M. Mauceri, D. Crippa, M. Albani, R. Bergamaschini, L. Miglio, F. La Via, *Mater. Des.* **2021**, *208*, 109833.
[35] A. G. Taboada, M. Meduňa, M. Salvalaglio, F. Isa, T. Kreiliger, C. V. Falub, E. Barthazy Meier, E. Müller, L. Miglio, G. Isella, H. von Känel, *J. Appl. Phys.* **2016**, *119*, 055301.
[36] F. Montalenti, F. Rovaris, R. Bergamaschini, L. Miglio, M. Salvalaglio, G. Isella, F. Isa, H. von Kanel, *Crystals* **2018**, *8*, 257.
[37] A. Heintz, B. Ilahi, A. Pofelski, G. Botton, G. Patriarche, A. Barzaghi, S. Fafard, R. Arès, G. Isella, A. Boucherif, *Nat. Commun.* **2022**, *13*, 6624.
[38] A. Barzaghi, S. Firoozabadi, M. Salvalaglio, R. Bergamaschini, A. Ballabio, A. Beyer, M. Albani, J. Valente, A. Voigt, D. J. Paul, L. Miglio, F. Montalenti, K. Volz, G. Isella, *Crystal Growth and Design* **2020**, *20*, 2914.
[39] R. Bergamaschini, F. Isa, C. Falub, P. Niedermann, E. Müller, G. Isella, H. von Känel, L. Miglio, *Surf. Sci. Rep.* **2013**, *68*, 390.
[40] M. Albani, R. Bergamaschini, A. Barzaghi, M. Salvalaglio, J. Valente, D. J. Paul, A. Voigt, G. Isella, F. Montalenti, *Sci. Rep.* **2021**, *11*, 18825
[41] C. Smith, J. Kirdoda, D. C. S. Dumas, Co. Coughlan, C. McCarthy, H. Mowbray, M. Mirza, F. Fleming, X. Yi, L. Saalbach, G. S. Buller, D. J. Paul, R. W. Millar, *Proceedings SPIE* **2023**, *12426*, 124260S.
[42] J. Pedrini, P. Biagioni, A. Ballabio, A. Barzaghi, M. Bonzi, E. Bonera, G. Isella, F. Pezzoli, *Opt. Express* **2020**, *28*, 24981.
[43] J. Pedrini, A. Barzaghi, J. Valente, D. J. Paul, G. Isella, F. Pezzoli, *Phys. Rev. Appl.* **2021**, *16*, 064024.
[44] V. Falcone, A. Ballabio, A. Barzaghi, C. Zucchetti, L. Anzi, F. Bottegoni, J. Frigerio, R. Sordan, P. Biagioni, G. Isella, *APL Photonics* **2022**, *7*, 046106.
[45] V. Falcone, *Il Nuovo Cimento C* **2022**, *45*, 203.
[46] D. Decoster, J. Harari, *Optoelectronic sensors*, John Wiley & Sons, xx **2013**
[47] S. Firoozabadi, P. Kükelhan, A. Beyer, J. Lehr, D. Heimes, K. Volz, *Ultramicroscopy* **2022**, *240*, 113550.
[48] L. Dieterle, B. Butz, E. Müller, *Ultramicroscopy* **2011**, *111*, 1636.